

Diffusion Representations for Fine-Grained Image Classification: A Marine Plankton Case Study

Aleix Nieto Juscafresa^{*†} Álvaro Mazcuñán Herreros[†] Josephine Sullivan
 KTH Royal Institute of Technology, Stockholm, Sweden
 {aleixnj, alvaromh, sullivan}@kth.se

Abstract

Diffusion models have emerged as state-of-the-art generative methods for image synthesis, yet their potential as general-purpose feature encoders remains underexplored. Trained for denoising and generation without labels, they can be interpreted as self-supervised learners that capture both low- and high-level structure. We show that a frozen diffusion backbone enables strong fine-grained recognition by probing intermediate denoising features across layers and timesteps and training a linear classifier for each pair. We evaluate this in a real-world plankton-monitoring setting with practical impact, using controlled and comparable training setups against established supervised and self-supervised baselines. Frozen diffusion features are competitive with supervised baselines and outperform other self-supervised methods in both balanced and naturally long-tailed settings. Out-of-distribution evaluations on temporally and geographically shifted plankton datasets further show that frozen diffusion features maintain strong accuracy and Macro F1 under substantial distribution shift.

1. Introduction

Diffusion models [25, 48, 50] have become a leading approach for generative modeling, delivering remarkable results in image synthesis [9, 15, 24] and extending to other modalities such as audio [29, 37], reinforcement learning [8, 19, 65], and computational biology [16, 59]. Through iterative denoising, diffusion models learn representations that capture global structure and fine-grained textures [62]. In their label-free training approach, they provide off-the-shelf, self-supervised features that transfer beyond generation and perform strongly in recognition tasks [15]. Furthermore, several works demonstrate that these features can remain discriminative even without task-specific tuning [28, 60]. Based on these findings, recent effort has gone into identifying which layers and timesteps are most dis-

criminative for classification and which representation details they capture, noting contrasts between fine-grained and more global features such as shape [28, 36].

Building on this line of work, we extend the analysis by evaluating diffusion representations in a *fine-grained* regime and by characterizing the link between generative quality and discriminative performance. In particular, we revisit layer and timestep selection under fine-grained recognition, quantify how fidelity affects classification accuracy, and diagnose when overfitting during diffusion-model training breaks this link. We therefore aim to answer two questions:

- *How well do pretrained diffusion features support fine-grained recognition across balanced and imbalanced training regimes?*
- *How are generation quality and the diffusion objective, including its per-timestep loss distribution, related to the discriminative strength of the resulting representations?*

To ground these questions in a fine-grained domain, we focus on plankton imagery. It poses an extreme fine-grained challenge with severe class imbalance (a few abundant taxa and a long tail of rare species), low contrast, and subtle inter-class variation [12].

Furthermore, beyond the technical challenge, *advances in plankton recognition directly benefit marine ecosystem monitoring*. This is because plankton communities control key ocean processes and serve as sensitive markers of climate-driven change, including warming, acidification, and shifting nutrient regimes [4, 10, 13]. To track these shifts at scale, automated instruments now produce massive, low-contrast image streams that must be classified by taxon to support abundance estimates and trend analysis [42, 44]. Labels are scarce and the task is fine-grained: taxa may differ only by slight changes, small spine or flagellum differences, and faint internal banding or vacuoles [12].

To address these challenges in low-contrast plankton imagery, we build on DDAE [60], a denoising diffusion feature extractor that requires no fine-tuning, to identify which U-Net decoder activations yield the highest linear-probe accuracy. We sweep decoder layers and timesteps, keep features frozen, and evaluate with a linear probe.

^{*}Corresponding author.

[†]Equal contribution.

We assess the layer-by-timestep readout across a curated class-balanced benchmark, a realistic long-tailed scenario with under-represented classes, and an out-of-distribution (OOD) test that transfers to a distinct plankton domain with unseen classes. In this out-of-distribution scenario, the source and target datasets differ in acquisition year, environmental and imaging conditions, and geographic location, so that the evaluation probes how robust the learned representations are. Across all three settings, our diffusion features outperform self-supervised baselines such as DINOv3 [47] under our evaluation protocol and are competitive with supervised baselines trained end-to-end, including Vision Transformers (ViTs) [11], ResNets [21], and EfficientNet [52]. By avoiding plankton-specific challenges [12], the study measures representation quality and provides practical guidance on where and when to select self-supervised features to support recognition effectively, including under realistic distribution shifts.

We summarize our main contributions as follows:

1. We formalize the general problem of selecting the optimal layer-timestep pair for feature selection, and, using a linear probe, we find a stable low-depth, moderate-noise region where diffusion features are most useful; we test this framework in fine-grained recognition.
2. We evaluate curated, imbalanced, and cross-distribution plankton regimes, amortizing compute by reusing pre-computed descriptors across related datasets, matching or surpassing strong supervised and self-supervised baselines.
3. We link generation quality to recognition, and to the optimal layer-timestep choice, by analyzing how the training objective and its noise-level loss schedule shape learned features.

2. Related Work

Fine-Grained Representations for Classification. Fine-grained classification hinges on capturing subtle, part-level distinctions, requiring representations that preserve local micro-patterns while integrating global context. For this task, attention mechanisms have proven especially effective: RA-CNN [14] sharpens part localization; CBAM [57] reweights spatial and channel cues; TransFG [20] uses token attention to surface discriminative parts; ViT [11] and CrossViT [6] capture long-range, multi-scale relations; bilinear pooling [33] isolates localized pairwise textures. In diffusion U-Nets, self-attention is applied at every denoising step, allowing distant regions to repeatedly exchange detail as noise is removed [9, 61]. This iterative process refines part correspondences and preserves fine texture, yielding compact, part-aware features that preserve micro-patterns under noise and clutter, motivating our use of frozen diffusion features for recognition [17, 38, 61].

Self-Supervised Learners for Representation. Self-supervised encoders learn without labels by exploiting image structure. Discriminative methods align crops from the same image; DINOv3 adds a momentum teacher, multi-crop views, centering/sharpening, and prototype assignments to yield robust, semantically organized features. Reconstruction methods predict missing content; MAE [22] masks a large patch fraction and reconstructs with a lightweight decoder, concentrating capacity in the encoder. These families differ in inductive bias: discriminative objectives promote invariance to viewpoint, color, and background, whereas reconstruction preserves fine detail and layout, which is useful for fine-grained and dense tasks.

Diffusion Model Representations. Diffusion models [25, 50] are trained for generation but are hypothesized to learn strong representations while denoising across many noise scales [15]. Competitive classification can be achieved by using intermediate activations without modifying the model [60]. Extending that idea, [39] identifies informative layers and noise levels and shows that aggregating across layers and timesteps improves linear separability. Low-dimensional latent spaces and structured noise schedules emerge as design factors for discriminative features [7]. Motivated by these observations, we study diffusion-derived features for plankton imagery, a low-contrast and fine-grained domain where such features have not been systematically evaluated. We report linear probes to measure representation quality independently of head capacity, following standard self-supervised practice used by DDAE [60] or DINOv3 [47].

Generative Approaches for Plankton Classification. Generative approaches for plankton classification have focused on augmentation and unsupervised representation learning, yet recognition gains remain limited. Conditional GANs synthesize minority taxa and report small improvements over convolutional baselines [34, 56]. CycleGAN increases the presence of rare Imaging FlowCytobot (IFCB) [54] taxa and can raise average precision once synthetic images are added to training [32, 34]. On very small algae collections, DCGAN with transfer learning improves accuracy after enlarging the training set, although effects are inconsistent across settings [1, 27, 45]. Beyond GANs, a VAE pipeline clusters plankton images by extracting DenseNet features without fine-tuning, learning a latent code with a VAE, and grouping the low-dimensional embeddings with fuzzy k -means, which reveals meaningful structure but does not establish clear benefits for supervised IFCB recognition [2]. Motivated by scarce labels and morphology-driven differences in plankton imagery, we evaluate diffusion-derived representations for recognition, a direction that, to our knowledge, has not been explored on IFCB data.

3. Background

We provide a brief overview of the original diffusion model formulation [25]. Since then, numerous variants have been proposed across its modular components, training objectives, noise parameterizations, and sampling procedures. For a detailed overview of these design choices, see [5].

Forward (noising) Process. Diffusion models [25, 41, 50] define a series of Gaussian corruptions on data x_0 . For timesteps $t = 1, \dots, T$, the corruption is described by the transition probability

$$q(x_t | x_{t-1}) = \mathcal{N}(\sqrt{\alpha_t} x_{t-1}, (1 - \alpha_t) \mathbf{I}), \quad (1)$$

where $\alpha_t \in (0, 1)$ sets the noise level. Conditioned on x_0 , the forward noising distribution at step t is $q(x_t | x_0) = \mathcal{N}(x_t; \sqrt{\bar{\alpha}_t} x_0, (1 - \bar{\alpha}_t) \mathbf{I})$, where $\bar{\alpha}_t = \prod_{s=1}^t \alpha_s$. Equivalently, using the reparameterization trick, a noised version of x_0 at an arbitrary level t can be obtained by sampling $\varepsilon \sim \mathcal{N}(0, \mathbf{I})$ and taking $x_t = \sqrt{\bar{\alpha}_t} x_0 + \sqrt{1 - \bar{\alpha}_t} \varepsilon$. When T is large, $x_T \approx \mathcal{N}(0, \mathbf{I})$. Common schedules choose α_t to vary smoothly (e.g., linear or cosine [41]).

Reverse (denoising) Process. At generation time we draw $x_T \sim \mathcal{N}(0, \mathbf{I})$ and iteratively denoise via $x_t \rightarrow x_{t-1}$. The one-step reverse law is the marginal over the unknown clean sample x_0 ,

$$q(x_{t-1} | x_t) = \int q(x_{t-1} | x_t, x_0) q(x_0 | x_t) dx_0. \quad (2)$$

Here $q(x_{t-1} | x_t, x_0)$ is Gaussian because, under the linear-Gaussian forward process, (x_{t-1}, x_t) are affine functions of x_0 plus Gaussian noise and hence jointly Gaussian; conditioning on x_0 preserves Gaussianity. The factor $q(x_0 | x_t)$ reflects uncertainty from the (unknown) data distribution, so the marginal above is a mixture and not tractable in closed form.

Because the forward step in Equation (1) is linear-Gaussian, small $\beta_t = 1 - \alpha_t$ makes each step an infinitesimal perturbation. In the continuous-time limit, time reversal yields a locally Gaussian reverse transition whose mean and covariance are determined by the score of the marginal q_t [48, 50]:

$$m(x_t, t) \approx \frac{1}{\sqrt{1 - \beta_t}} \left(x_t + \beta_t \nabla_{x_t} \log q_t(x_t) \right) \quad (3)$$

$$\text{Cov} \approx \beta_t \mathbf{I}, \quad (4)$$

where “ \approx ” denotes a small-step surrogate for the discrete transition (it does *not* claim the unconditional discrete transition is exactly Gaussian).

At the actual discrete step $t \rightarrow t - 1$, conditioning on x_0 makes (x_{t-1}, x_t) jointly Gaussian because they are affine

functions of x_0 and Gaussian noises; therefore the conditional reverse posterior is Gaussian with density $q(x_{t-1} | x_t, x_0) = \mathcal{N}(x_{t-1}; \tilde{\mu}_t(x_t, x_0), \tilde{\beta}_t \mathbf{I})$, where

$$\tilde{\mu}_t(x_t, x_0) = \frac{\sqrt{\alpha_t} (1 - \bar{\alpha}_{t-1})}{1 - \bar{\alpha}_t} x_t + \frac{\sqrt{\bar{\alpha}_{t-1}} \beta_t}{1 - \bar{\alpha}_t} x_0, \quad (5)$$

$$\tilde{\beta}_t = \frac{\beta_t (1 - \bar{\alpha}_{t-1})}{1 - \bar{\alpha}_t}. \quad (6)$$

Thus the *per-step* variance $\tilde{\beta}_t \mathbf{I}$ is exact and depends only on the schedule, not on x_t or x_0 ; a Taylor expansion shows $\tilde{\beta}_t = \beta_t - \frac{\bar{\alpha}_{t-1}}{1 - \bar{\alpha}_{t-1}} \beta_t^2 + O(\beta_t^3) = \beta_t + O(\beta_t^2)$. In practice we keep this variance fixed and compute the mean by plugging in a learned estimate $\hat{x}_0(x_t, t)$ obtained next:

$$p_\theta(x_{t-1} | x_t) = \mathcal{N}(x_{t-1}; \tilde{\mu}_t(x_t, \hat{x}_0(x_t, t)), \tilde{\beta}_t \mathbf{I}). \quad (7)$$

Noise Prediction (training objective). We parameterize a *network* $E_\theta(x_t, t)$ to predict the Gaussian noise used to form x_t and train it with the standard MSE $\mathcal{L}_{\text{noise}}(\theta) = \mathbb{E}_{t, x_0, \varepsilon} [\|\varepsilon - E_\theta(x_t, t)\|_2^2]$. From E_θ we recover an estimate of the clean sample $\hat{x}_0(x_t, t) = x_t - \sqrt{1 - \bar{\alpha}_t} E_\theta(x_t, t) / \sqrt{\bar{\alpha}_t}$, which is then substituted into $\tilde{\mu}_t(x_t, x_0)$ to produce the mean of $p_\theta(x_{t-1} | x_t)$ used during sampling. Equivalently, we may write the sampling mean directly in terms of the predicted noise as

$$\mu_\theta(x_t, t) = \tilde{\mu}_t(x_t, \hat{x}_0(x_t, t)) \quad (8)$$

$$= \frac{1}{\sqrt{\alpha_t}} \left(x_t - \frac{\beta_t}{\sqrt{1 - \bar{\alpha}_t}} E_\theta(x_t, t) \right) \quad (9)$$

Sampling (iterative process). Starting from a pure noise sample $x_T \sim \mathcal{N}(0, \mathbf{I})$, use the learned Gaussian $p_\theta(x_{t-1} | x_t) = \mathcal{N}(\mu_\theta(x_t, t), \tilde{\beta}_t \mathbf{I})$ and update $x_{t-1} \leftarrow \mu_\theta(x_t, t) + \tilde{\beta}_t^{1/2} z$, $z \sim \mathcal{N}(0, \mathbf{I})$.

This is the original DDPM sampler [25]; many improved variants exist [5].

Diffusion Feature Extraction. The most common way of obtaining features is by first corrupting an input image to a chosen noise level t to form x_t and forwarding (x_t, t) through a pretrained U-Net denoiser. Feature maps are read at the outputs of selected decoder residual blocks, providing multi-scale descriptors without updating model weights [3, 40, 53, 63, 64]. Typical diffusion timesteps used in prior work include $t = 45$ [60], $t = 50$ [64] or $t = 261$ [53]. Complementary to this noised-input paradigm, CleanDIFT shows that a lightweight, unsupervised fine-tuning of the diffusion backbone enables the extraction of high-quality semantic features directly from clean images—surpassing noise-augmented and even ensemble-based extraction at a fraction of the computational cost [51].

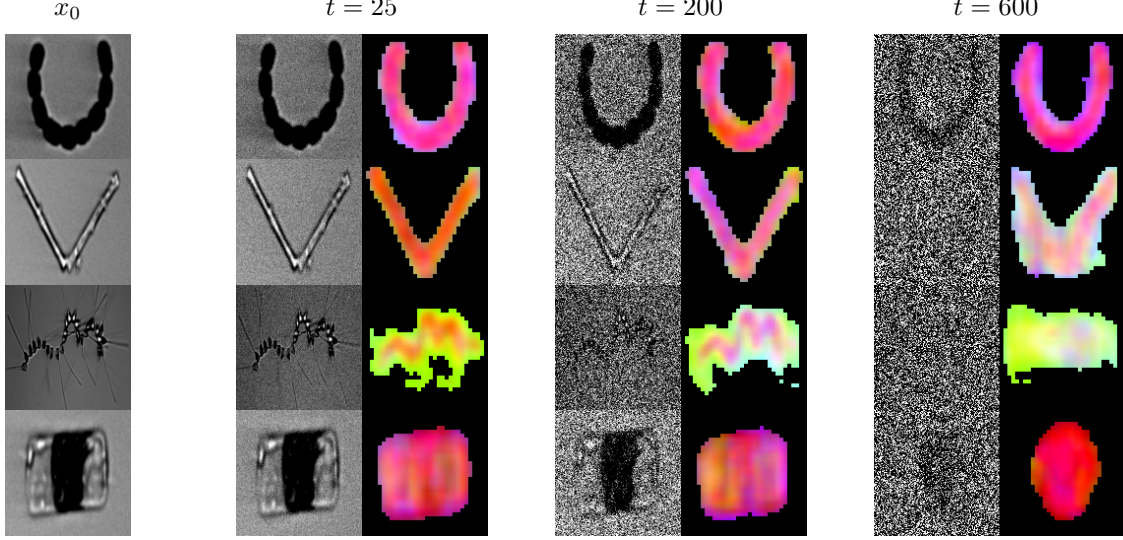


Figure 1. Principal Component Analysis (PCA) visualization of diffusion features. Using random samples, we compute PCA on the diffusion features and map the first three principal components to the RGB channels. For each sample, we show the clean target image and its noisy versions at timesteps $t \in \{25, 200, 600\}$ with the corresponding PCA colorization overlaid on the noisy image. Background regions are suppressed by masking pixels with low values on the first principal component. This visualization is inspired by [43].

4. Methodology

We use a diffusion model whose denoiser is a U-Net *backbone* [46] with an encoder-bottleneck-decoder topology and skip connections. The U-Net is trained on our dataset (no pretraining) following the *noise prediction* objective [25]. For a variance schedule $\{\beta_t\}_{t=1}^T$ with $\alpha_t = 1 - \beta_t$ and *cumulative signal coefficient* $\bar{\alpha}_t = \prod_{s=1}^t \alpha_s$, the forward noising process [25] is $x_t = \sqrt{\bar{\alpha}_t} x_0 + \sqrt{1 - \bar{\alpha}_t} \varepsilon$, $\varepsilon \sim \mathcal{N}(0, \mathbf{I})$, where x_t is the noised $x_0 \sim p_{\text{data}}$ and t indexes the noise level. Let $E_\theta(x_t, t)$ denote the noise estimator. The loss is

$$\mathcal{L}_{\text{noise}}(\theta) = \mathbb{E}_{t, x_0, \varepsilon} \left[w(t) \left\| \varepsilon - E_\theta(x_t, t) \right\|_2^2 \right], \quad (10)$$

where $w(t) > 0$ is a per-step weight, and the diffusion step t is sampled from a discrete distribution $t \sim p(t)$ on $\{1, \dots, T\}$.

4.1. Decoder Stage Activations

Let E_θ denote the trained U-Net denoiser. During inference for representation extraction, we freeze E_θ so it acts purely as a *feature extractor*. Then, for a chosen noise level t , we construct x_t from x_0 via the forward noising process and write $x_t(x_0)$ to make the dependence on the original image explicit. We feed both $x_t(x_0)$ and the same t to E_θ , ensuring the *conditioning matches the corruption level whose noise the model was trained to predict*. Throughout, we treat t as an explicit conditioning variable: features are always extracted from the denoiser under the same noise level at which the input was corrupted.

Readout Locations and Indexing. We extract decoder features after each residual block. The decoder contains four stages with different resolutions $\{16^2, 32^2, 64^2, 128^2\}$ with three residual blocks per stage (RB1–RB3), giving 12 readout locations. We index these locations by a single flattened index $\ell \in \{1, \dots, 12\}$, mapping (r, b) to ℓ via $\ell = 3(r-1) + b$, where $r \in \{1, 2, 3, 4\}$ denotes the decoder stage (from 16^2 to 128^2) and $b \in \{1, 2, 3\}$ denotes the residual block (RB1–RB3).

A decoder forward pass with inputs $(x_t(x_0), t)$ yields the readout activation at location ℓ :

$$z^{(\ell)}(x_0, t) = u^{(\ell)}(x_t(x_0), t) \in \mathbb{R}^{C_\ell \times H_\ell \times W_\ell}, \quad (11)$$

where $u^{(\ell)}(\cdot, \cdot)$ denotes the corresponding activation mapping in the frozen *decoder* of E_θ , evaluated at $(x_t(x_0), t)$. Here C_ℓ, H_ℓ, W_ℓ are the channel count and spatial resolution of the feature tensor at readout location ℓ . In particular, $H_\ell = W_\ell \in \{16, 32, 64, 128\}$ depending on the decoder stage, and C_ℓ follows the decoder channel width at that stage.

To obtain a fixed-dimensional descriptor suitable for linear probing, we convert each feature tensor to a vector by spatial pooling. The corresponding embedding is obtained by *global average pooling*:

$$\phi_{t, \ell}(x_0) = \text{GAP}(z^{(\ell)}(x_0, t)) \in \mathbb{R}^{C_\ell}. \quad (12)$$

This produces one feature vector per image, timestep, and readout location, enabling a controlled comparison of discriminative quality across the (t, ℓ) grid while keeping the downstream classifier capacity fixed.

Attention Placement. We insert a single self-attention module at the 16^2 decoder stage (also in the encoder). At that stage, the final residual block includes this attention module, and we read features after it. All other readout locations correspond to purely convolutional residual blocks. Concretely, this design ensures that one readout location captures attention-augmented global interactions at an intermediate spatial grid, while the remaining readouts measure the contribution of convolutional processing alone at multiple resolutions.

Why the Decoder? We place the attention readout in the decoder rather than the encoder or bottleneck for three reasons. First, decoder activations merge U-Net encoder features from the skip connections with conditioning on the current noise level t , producing representations that jointly capture local morphology and the progressively denoised global context most relevant for recognition. Second, at moderate and high t the U-Net encoder is dominated by corrupted inputs, which lowers the signal-to-noise ratio for fine structures; in contrast, the decoder operates on features produced by the denoiser conditioned on noise level t , which are trained to predict denoising directions. Third, the bottleneck is deliberately narrow and global: it is well suited for coordinating the generative process but tends to suppress the part-level cues required for fine-grained discrimination. Empirically, this inductive bias is consistent with the linear probe results in Section 5.1, where decoder attention readouts yield the strongest separability across species.

4.2. Linear Probe and Final Representation

Using the decoder features $\phi_{t,\ell}$ defined in Equation (12) as embeddings, we assess linear separability across (t, ℓ) via a *linear probe* (linear softmax classifier) fitted independently at each (t, ℓ) . With training data $\mathcal{D}_{\text{tr}} = \{(x_{0,i}, y_i)\}_{i=1}^n$ and test data $\mathcal{D}_* = \{(x_{0,i}^*, y_i^*)\}_{i=1}^{n_*}$, we set the embedding $\phi_{t,\ell}(x_0)$ and fit $f_{t,\ell}(x_0) = W\phi_{t,\ell}(x_0) + b$ by minimizing the cross-entropy loss function

$$\mathcal{L}_{\text{CE}}(W, b) = \frac{1}{n} \sum_{i=1}^n -\log(\text{softmax}_{y_i}(f_{t,\ell}(x_{0,i}))). \quad (13)$$

We evaluate $\text{Acc}_*(f_{t,\ell})$ on \mathcal{D}_* and choose $(t^*, \ell^*) \in \arg \max_{t,\ell} \text{Acc}_*(f_{t,\ell})$, i.e., the (t, ℓ) whose linear probe achieves the highest discriminative accuracy across layers and timesteps in the validation set. The final feature used for downstream tasks is then

$$\phi(x_0) = \phi_{t^*, \ell^*}(x_0) \in \mathbb{R}^{C_{\ell^*}}. \quad (14)$$

The intuition behind these representations is to capture the most informative patterns that E_θ has learned when denoising at t^* .

4.3. Training Objective and Loss Weighting

We train E_θ as an *unconditional* denoiser on the training split using the objective in Equation (10). The forward process is discretized into $T = 1000$ diffusion steps with a cosine noise schedule. For the timestep weighting $w(t)$ we consider two variants:

$$w_{\text{MSE}}(t) = 1, \quad (15)$$

$$w_{\text{MinSNR}}(t) = \frac{\min(\text{SNR}(t), \gamma)}{\text{SNR}(t)}. \quad (16)$$

Here $\text{SNR}(t)$ denotes the *signal-to-noise* ratio at diffusion step t under the forward process, defined as

$$\text{SNR}(t) = \frac{\bar{\alpha}_t}{1 - \bar{\alpha}_t}. \quad (17)$$

Unless otherwise stated, we train E_θ with $\text{MinSNR-}\gamma$ weighting $w_{\text{MinSNR}}(t)$, which downweights high-SNR (near-clean) timesteps relative to uniform MSE $w_{\text{MSE}}(t) \equiv 1$ by setting $w_{\text{MinSNR}}(t) = \min(\text{SNR}(t), \gamma)/\text{SNR}(t)$.

Optimization uses AdamW (learning rate $5 \cdot 10^{-4}$, $\beta_1 = 0.9$, $\beta_2 = 0.999$, weight decay 10^{-4}), cosine learning-rate decay with a 5% warmup, global gradient clipping at 1.0, mixed-precision training, and an exponential moving average of parameters with decay 0.999. We train for 250 epochs with a batch size of 256 and select the checkpoint with the lowest validation loss (epoch 100). Class labels are *never* used during denoiser training.

5. Experiments & Results

We evaluate our method on two datasets formed by Imaging FlowCytobot (IFCB) images from the SMHI [54] and SYKE [30] Baltic programs. After preprocessing (see Appendix A), we obtain (i) a balanced dataset with $k = 70$ classes, where each class contributes 500 single-channel grayscale images resized to 128×128 pixels, and (ii) an unbalanced dataset with 120 classes and varying numbers of images per class. For each dataset, we construct class-stratified training and validation splits and keep a separate held-out split. The diffusion model is trained only on the training split. The validation split is used to track the diffusion loss, monitor generative quality via Fréchet Inception Distance (FID) [23], computed by replicating grayscale ROIs to three channels and using the standard Inception-V3 feature extractor, and select the network layer and diffusion timestep for representation extraction by linear probing; *labels are never used during diffusion training*. The held-out test split, a fixed non-stratified subset without data augmentation, is used only for final downstream evaluation, where we report test accuracy and Macro F1 from the linear probe using the layer-timestep pair chosen on the validation set. Complete implementation details, including the diffusion-model architecture, linear probe configuration, and all hyperparameters, are provided in Appendix B.

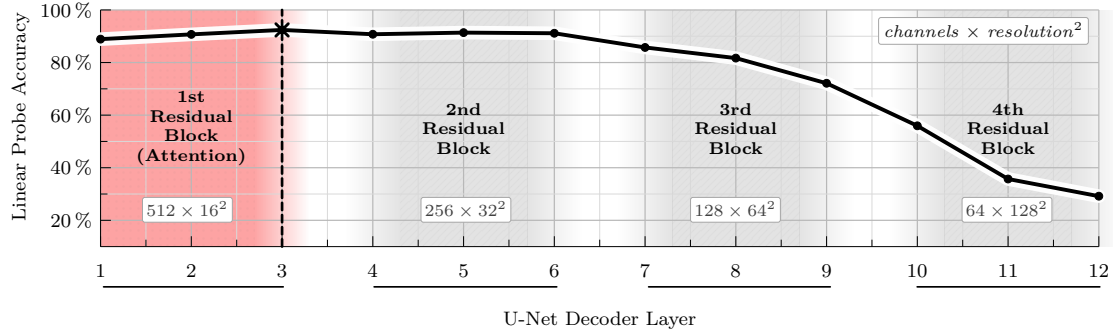


Figure 2. Linear probe accuracy across decoder readout locations $\ell \in \{1, \dots, 12\}$ at the optimal noise level $t^* = 25$. The DDPM runs for $T = 1000$ total timesteps, and we probe the subset $\{1, 10, 25, 50, 75, 100, 200, 400, 600\}$.

5.1. Linear Probe Discriminant Analysis

To select the final diffusion representation, we sweep the U-Net decoder readout locations ℓ and denoising timesteps $t \in \{1, 10, 25, 50, 75, 100, 200, 400, 600\}$. For each pair (t, ℓ) we extract activations as defined in Section 4.2, fit a linear softmax classifier on the corresponding training representations, and use validation accuracy to select (t^*, ℓ^*) following Section 4.2. The best-performing probe is obtained for $t^* = 25$ at the decoder readout location $\ell^* = 3$ (RB3 at resolution 16^2 under our flattening), so $(t^*, \ell^*) = (25, 3)$. This indicates that features at this stage already support near-linear class separation, combining global context from self-attention with a compact spatial grid (16×16) and high channel capacity (512). As shown in Figure 2, probe accuracy decreases for later decoder blocks (higher spatial resolution, lower channel count), suggesting subsequent upsampling prioritizes synthesis over linear separability. Full linear probe results are in Appendix C.

5.2. Baselines

To contextualize our approach, we compare against supervised and self-supervised baselines. Supervised models include ResNet-50 [21], EfficientNet-B0/B3/V2-S [52], and ViT-B/16 [11] trained end-to-end with cross-entropy on the target training split, as well as a lightweight MLP on hand-crafted features (SIFT [35] and edges). For self-supervised baselines, we start from ImageNet-1k pretrained MAE [22] and DINOv3 [47] (ViT-B/16) and fine-tune the backbones on the target training images using their self-supervised objectives (no labels). We then freeze these fine-tuned backbones and train a linear probe on the target training split; the validation split is used for model selection (including any probe hyperparameters), and we report final results on the held-out test split. Our diffusion model is trained unconditionally from scratch on the target training images without labels and evaluated with the same frozen-feature linear-probe protocol. In Table 1, we report the resulting metrics and parameter counts.

5.3. Distribution Shift

We assess out-of-distribution generalization using two unseen IFCB datasets. The first dataset [30] is a year-long Baltic Sea collection acquired over a different 12-month period than our training data, spanning a broad range of seasonal and environmental conditions. The second is WHOI-22 [44] from the U.S. Atlantic coast, which differs geographically and taxonomically. In all cases, we freeze the diffusion backbone and train only a linear classifier on top of the extracted features using the target dataset’s training split, and we report performance on the corresponding target test split. No target-domain images or labels are used to train the diffusion backbone; only the linear classifier is trained using target labels.

Our features exhibit strong transfer under both types of distribution shift, as shown in Table 2. Overall accuracy is largely driven by the most frequent taxa, whereas Macro F1 averages performance across classes and is therefore much more sensitive to rare taxa. Because both Baltic (OOD) and WHOI-22 are naturally long-tailed, with several rare or weakly represented classes, accuracy can remain relatively high even when Macro F1 is lower, since reduced recall and precision on minority taxa has a limited effect on accuracy. This behavior is visible in Table 2: performance remains robust under both temporal shift (Baltic) and geographic shift (WHOI-22), with a larger decrease in Macro F1 under the more challenging WHOI-22 shift.

Table 2. Out-of-distribution linear-probe evaluation on frozen diffusion features. The training regime denotes which source dataset was used to train the diffusion model weights. Metrics are computed on each target dataset’s label set.

Dataset	Training regime	Accuracy	Macro F1
Baltic (OOD)	Balanced	0.9133	0.7356
	Unbalanced	0.9112	0.7564
WHOI-22	Balanced	0.8411	0.8392
	Unbalanced	0.8272	0.8260

Table 1. Linear probe accuracy and Macro F1 on our balanced/unbalanced datasets for supervised baselines, self-supervised models, and our diffusion-based representation. Bold indicates the best result within groups, and \uparrow (\downarrow) indicate metrics where higher (lower) is better.

Model	Balanced Dataset		Unbalanced Dataset		
	Accuracy \uparrow	Macro F1 \uparrow	Accuracy \uparrow	Macro F1 \uparrow	Params \downarrow
<i>Supervised Methods</i>					
MLP on features	0.7602	0.7206	0.8651	0.7027	0.1M
ResNet-50	0.9281	0.9229	0.9759	0.8864	25.5M
EfficientNet-B0	0.9490	0.9455	0.9761	0.8994	4M
EfficientNet-B3	0.9508	0.9447	0.9613	0.8421	11M
EfficientNet-V2-S	0.9302	0.9257	0.9100	0.9050	22.5M
ViT-B/16	0.9209	0.9128	0.9050	0.8980	87M
<i>Self-Supervised Methods</i>					
Masked Autoencoders (ViT-B/16)	0.8467	0.8214	0.8207	0.8001	87M
DINOv3 (ViT-B/16)	0.8031	0.6145	0.7909	0.3274	87M
Our Diffusion	0.9240	0.9114	0.9145	0.9064	57M

For OOD evaluation, we freeze the diffusion backbone trained on the source regime and extract features for all target images. We then train a linear classifier on the target dataset’s training split using the target labels and evaluate on the target test split. We do not restrict evaluation to only classes shared with the source training set, *since the backbone can produce features for any input image* and the linear probe can be trained to predict the target labels from these frozen features. This protocol isolates representation transfer under distribution shift because the diffusion model weights remain fixed and only the lightweight linear probe is fit on the target domain. Moreover, because target class frequencies can differ substantially from the source regimes, this evaluation reflects performance under realistic long-tailed distributions.

5.4. Ablation Studies

Loss Function Ablation. We study how the training objective shapes the linear probe quality of diffusion features across noise levels. Specifically, we consider loss function (10) objectives that differ only in how they weight timesteps t in the denoising loss. The first is the standard uniform MSE weighting, $w_{\text{MSE}}(t) \equiv 1$, and the second is the weighting $w_{\text{MinSNR}}(t)$ [18]. Under uniform MSE, the mean-squared error allocates substantial weight to both very easy high-SNR and hard low-SNR conditions, which can under-train the mid-SNR regime where much of the denoising trajectory resides. In contrast, MinSNR- γ weighting with $\gamma = 5$ counteracts this by capping the contribution of extreme SNRs and emphasizing the informative middle of the schedule. As shown in Figure 4, features learned with MinSNR- γ maintain classification accuracy as SNR decreases, and in the high-SNR (early) regime they show a slight improvement, whereas on our IFCB plankton experiments, features learned with uniform MSE degrade steadily.

Generation Fidelity. During training we monitored both FID and validation loss and found that they decouple: after a certain point, validation loss shows clear overfitting while FID continues to improve. This behavior arises because FID measures proximity between generated samples and the validation distribution, which in our setting is close to the training distribution; as the generator memorizes training statistics, sample quality by FID can keep rising even as the model overfits and its representations degrade. To verify the effect on downstream utility, we compared an overfit checkpoint with a better FID to a checkpoint selected by the minimum validation loss. Linear probing on frozen features revealed an accuracy drop from 0.9240 to 0.8812, roughly a four-point absolute decline, for the overfit model. These results, detailed in Appendix C, suggest that FID is useful as a diagnostic but should not be the optimization target when training diffusion models for representation learning on fine-grained classification tasks.

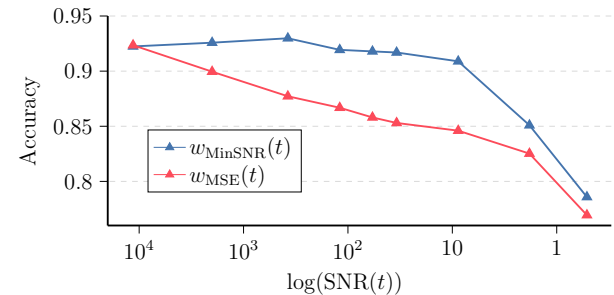


Figure 4. Effect of loss on linear probe accuracy across noise. Linear probe accuracy as a function of $\log \text{SNR}(t)$ for the best decoder readout (t^*, ℓ^*) . We compare two denoisers trained with identical architecture and schedule but different timestep weightings: uniform MSE weighting $w_{\text{MSE}}(t) \equiv 1$ and MinSNR ($\gamma=5$) weighting $w_{\text{MinSNR}}(t)$. High SNR corresponds to nearly clean inputs, low SNR to heavily noised inputs. Balanced dataset.

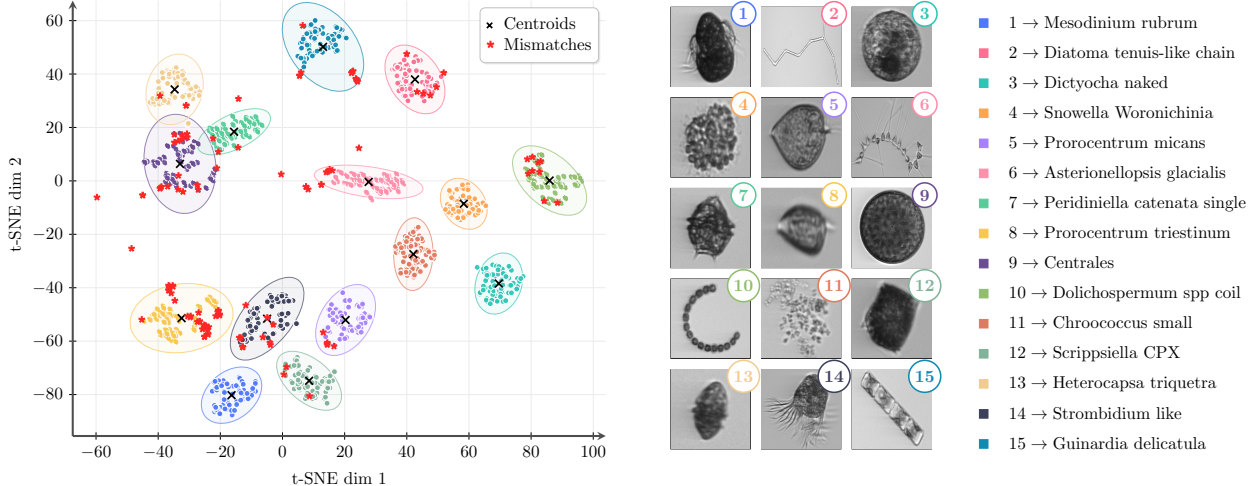


Figure 3. Visualization of learned representations via t-SNE with k -means (15 out of the 70 classes), with clusters matched to labels using the *Hungarian algorithm* [31]. Mismatches represent points of the selected labels that did not fall under the correct cluster.

5.5. Clustering as a Diagnostic

Beyond the linear probe, we examine class-consistent structure by running k -means (balanced dataset) with $k = 70$ on *test* embeddings $\phi(x_0)$ extracted at (t^*, ℓ^*) . This analysis complements the linear probe, which directly evaluates linear separability, *by probing structure in the absence of supervision* [2]. Figure 3 presents a 2D t-SNE embedding of the learned representations for a subset of visually similar plankton classes, annotated with k -means partitions, to assess fine-grained class separability. The visualization reveals both well-separated and overlapping regions, highlighting where the model confuses classes and how the feature space organizes taxonomically coherent groupings. A more comprehensive set of clustering metrics is provided in Appendix C.

6. Discussions

We extract representations from a frozen diffusion backbone by reading decoder activations at multiple depths and noise timesteps. For each (t, ℓ) , we train a linear classifier to measure linear separability and select the pair that maximizes validation accuracy. Across our settings, the most discriminative features consistently arise in early decoder readouts at small-to-moderate noise levels, where the representation retains intermediate-level shape and texture while suppressing overly fine, instance-specific details. This aligns with the intuition that high noise preserves only coarse structure, whereas very low noise reintroduces fine-scale variation that is less stable for linear separation. In our experiments, the best probe accuracy is obtained at the selected readout corresponding to the final attention-equipped decoder block, suggesting that late attention refines class-relevant cues without collapsing the representation into sample-specific detail.

Across experiments, the $\text{MinSNR-}\gamma$ objective shifts learning toward slightly noisier timesteps, producing more noise-robust, morphology-preserving representations and improving linear probing on fine-grained plankton images. We also find that higher generative quality doesn't necessarily translate to better discriminative performance, so the two should be evaluated separately.

These observations yield a practical guideline for our setting: use a single early to mid layer feature at low noise from a frozen backbone and train only a linear probe. This keeps adaptation lightweight, reduces instrument-specific overfitting, and supports transfer by reusing the same features across datasets. Although diffusion training is costlier than CNNs, the cost is amortized by reusing the backbone and only refitting the probe per dataset.

Our experiments use IFCB plankton images, but the feature extractor is self-supervised and makes no instrument- or dataset-specific assumptions. It learns from raw images without microscopy rules, hand-crafted features, or acquisition priors; labels are used only by the downstream classifier. As a result, the same representation supports competitive linear probes compared with strong supervised baselines and clearly outperforms ViT-based self-supervised baselines, and it transfers to other labeled plankton collections and environmental microscopy datasets.

Are Diffusion Models Learning Morphology? When extracting representations, we use the decoder block selected by the linear probe and treat all its spatial locations across a batch of plankton images as feature tokens. Running PCA on these tokens and mapping the first three components to RGB yields the overlays in Figure 1, where consistent colors along each organism across noise levels suggest that diffusion features are organized by plankton morphology rather than raw pixel values.

Runtime and Memory. We train our diffusion model for 15 h on $4 \times$ NVIDIA A100-40GB GPUs on a single node. Peak GPU memory usage is ~ 38 GB per GPU. Training uses 24 CPU threads and ≈ 11 GB of disk space for checkpoints and logs.

Limitations & Extensions. A limitation of this study is that the above findings on layer-timestep selection and the location of the most discriminative decoder features are established for a single U-Net family, a fixed attention placement, and the noise schedules we evaluate on IFCB plankton imagery; extending the same sweep to additional architectures, schedules, and datasets would be required to claim broader stability. This work is also limited to a single Baltic site and grayscale ROI imagery, so conclusions are environment- and acquisition-specific.

Data-wise, next steps are to test whether diffusion-based representations outperform standard CNNs on heavily imbalanced data and to quantify how augmentation reduces imbalance by stratifying noise-prediction loss by augmentation, probing timestep- and decoder-wise invariances with linear probes and k -means retrieval in a shared embedding space, and using padding diagnostics to separate biological signal from instrument artifacts.

Model-wise, directions include pretraining and fine-tuning, cross-instrument adaptation, and alternative diffusion designs such as latent diffusion and EDM-style schedules [26]; ablating the timestep-sampling distribution $p(t)$ (we use squared-cosine importance sampling) and its interaction with $\text{MinSNR-}\gamma$ to disentangle sampling effects from loss reweighting, for example by comparing against uniform timestep sampling; replacing FID with metrics that disentangle fidelity from coverage; tracking noise-prediction loss across timesteps and relating it to held-out quality to distinguish structure learning from texture memorization and detect overfitting; recognizing that clustering uses representations chosen with supervised timestep/layer selection and is therefore not a label-free baseline; and studying concatenated multi-step features, attention placement, and linear probe plus attribution analyses beyond raw attention to localize class-separable, task-relevant signals.

References

- [1] Abdullah, Sikandar Ali, Ziaullah Khan, Ali Hussain, Ali Athar, and Hee-Cheol Kim. Computer Vision Based Deep Learning Approach for the Detection and Classification of Algae Species Using Microscopic Images. *Water*, 14(14):2219, 2022. [2](#)
- [2] Paolo Didier Alfano, Marco Rando, Marco Letizia, Francesca Odone, Lorenzo Rosasco, and Vito Paolo Pastore. Efficient Unsupervised Learning for Plankton Images. In *2022 26th International Conference on Pattern Recognition (ICPR)*, pages 1314–1321. IEEE, 2022. [2](#), [8](#)
- [3] Dmitry Baranchuk, Ivan Rubachev, Andrey Voynov, Valentin Khrulkov, and Artem Babenko. Label-Efficient Semantic Segmentation with Diffusion Models. *arXiv preprint arXiv:2112.03126*, 2021. [3](#)
- [4] Gregory Beaugrand, Philip C Reid, Frédéric Ibañez, J Alastair Lindley, and Martin Edwards. Reorganization of North Atlantic Marine Copepod Biodiversity and Climate. *Science*, 296(5573):1692–1694, 2002. [1](#)
- [5] Hanqun Cao, Cheng Tan, Zhangyang Gao, Yilun Xu, Guangyong Chen, Pheng-Ann Heng, and Stan Z Li. A Survey on Generative Diffusion Models. *IEEE Transactions on Knowledge and Data Engineering*, 36(7):2814–2830, 2024. [3](#)
- [6] Chun-Fu Richard Chen, Quanfu Fan, and Rameswar Panda. CrossViT: Cross-Attention Multi-Scale Vision Transformer for Image Classification. In *Proceedings of the IEEE/CVF International Conference on Computer Vision*, pages 357–366, 2021. [2](#)
- [7] Xinlei Chen, Zhuang Liu, Saining Xie, and Kaiming He. Deconstructing Denoising Diffusion Models for Self-supervised Learning. *arXiv preprint arXiv:2401.14404*, 2024. [2](#)
- [8] Cheng Chi, Zhenjia Xu, Siyuan Feng, Eric Cousineau, Yilun Du, Benjamin Burchfiel, Russ Tedrake, and Shuran Song. Diffusion Policy: Visuomotor Policy Learning via Action Diffusion. *The International Journal of Robotics Research*, 44(10-11):1684–1704, 2025. [1](#)
- [9] Prafulla Dhariwal and Alexander Nichol. Diffusion models Beat GANs on Image Synthesis. *Advances in neural information processing systems*, 34:8780–8794, 2021. [1](#), [2](#), [17](#)
- [10] Scott C Doney, Victoria J Fabry, Richard A Feely, and Joan A Kleypas. Ocean Acidification: the Other CO₂ Problem. *Annual Review of Marine Science*, 1(1):169–192, 2009. [1](#)
- [11] Alexey Dosovitskiy. An Image is Worth 16x16 Words: Transformers for Image Recognition at Scale. *arXiv preprint arXiv:2010.11929*, 2020. [2](#), [6](#)
- [12] Tuomas Eerola, Daniel Batrakhanov, Nastaran Vatankhah Barazandeh, Kaisa Kraft, Lumi Haraguchi, Lasse Lensu, Sanna Suikkanen, Jukka Seppälä, Timo Tamminen, and Heikki Kälviäinen. Survey of Automatic Plankton Image Recognition: Challenges, Existing Solutions and Future Perspectives. *Artificial Intelligence Review*, 57(5):114, 2024. [1](#), [2](#)
- [13] Paul G Falkowski, Richard T Barber, and Victor Smetacek. Biogeochemical Controls and Feedbacks on Ocean Primary Production. *Science*, 281(5374):200–206, 1998. [1](#)
- [14] Jianlong Fu, Heliang Zheng, and Tao Mei. Look Closer to See Better: Recurrent Attention Convolutional Neural Network for Fine-grained Image Recognition. In *Proceedings of the IEEE Conference on Computer Vision and Pattern Recognition*, pages 4438–4446, 2017. [2](#)
- [15] Michael Fuest, Pingchuan Ma, Ming Gui, Johannes Schusterbauer, Vincent Tao Hu, and Bjorn Ommer. Diffusion Models and Representation Learning: A Survey. *arXiv preprint arXiv:2407.00783*, 2024. [1](#), [2](#), [17](#)
- [16] Nate Gruver, Samuel Stanton, Nathan Frey, Tim GJ Rudner, Isidro Hotzel, Julien Lafrance-Vanassee, Arvind Rajpal, Kyunghyun Cho, and Andrew G Wilson. Protein Design

with Guided Discrete Diffusion. *Advances in Neural Information Processing Systems*, 36:12489–12517, 2023. 1

[17] Andi Han, Wei Huang, Yuan Cao, and Difan Zou. On the Feature Learning in Diffusion Models. *arXiv preprint arXiv:2412.01021*, 2024. 2

[18] Tiankai Hang, Shuyang Gu, Chen Li, Jianmin Bao, Dong Chen, Han Hu, Xin Geng, and Baining Guo. Efficient Diffusion Training via Min-SNR Weighting Strategy. In *Proceedings of the IEEE/CVF International Conference on Computer Vision*, pages 7441–7451, 2023. 7, 17

[19] Philippe Hansen-Estruch, Ilya Kostrikov, Michael Janner, Jakub Grudzien Kuba, and Sergey Levine. IDQL: Implicit Q-Learning as an Actor-Critic Method with Diffusion Policies. *arXiv preprint arXiv:2304.10573*, 2023. 1

[20] Ju He, Jie-Neng Chen, Shuai Liu, Adam Kortylewski, Cheng Yang, Yutong Bai, and Changhu Wang. TransFG: A Transformer Architecture for Fine-Grained Recognition. In *Proceedings of the AAAI Conference on Artificial Intelligence*, pages 852–860, 2022. 2

[21] Kaiming He, Xiangyu Zhang, Shaoqing Ren, and Jian Sun. Deep Residual Learning for Image Recognition. In *Proceedings of the IEEE Conference on Computer Vision and Pattern Recognition*, 2016. 2, 6

[22] Kaiming He, Xinlei Chen, Saining Xie, Yanghao Li, Piotr Dollár, and Ross Girshick. Masked Autoencoders Are Scalable Vision Learners. In *Proceedings of the IEEE/CVF conference on computer vision and pattern recognition*, pages 16000–16009, 2022. 2, 6

[23] Martin Heusel, Hubert Ramsauer, Thomas Unterthiner, Bernhard Nessler, and Sepp Hochreiter. GANs Trained by a Two Time-Scale Update Rule Converge to a Local Nash Equilibrium. *Advances in Neural Information Processing Systems*, 30, 2017. 5

[24] Jonathan Ho and Tim Salimans. Classifier-free diffusion guidance. *arXiv preprint arXiv:2207.12598*, 2022. 1

[25] Jonathan Ho, Ajay Jain, and Pieter Abbeel. Denoising Diffusion Probabilistic Models. *Advances in Neural Information Processing Systems*, 33:6840–6851, 2020. 1, 2, 3, 4

[26] Tero Karras, Miika Aittala, Timo Aila, and Samuli Laine. Elucidating the Design Space of Diffusion-Based Generative Models. *Advances in Neural Information Processing Systems*, 35:26565–26577, 2022. 9

[27] Ziaull Khan, Wajid Mumtaz, Abdul Samad Mumtaz, Subrata Bhattacharjee, Hee-Cheol Kim, et al. Multiclass Classification of Algae Using DCGAN and Transfer Learning. In *2022 2nd International Conference on Image Processing and Robotics (ICIPRob)*, pages 1–6. IEEE, 2022. 2

[28] Dahye Kim, Xavier Thomas, and Deepthi Ghadiyaram. Revolio: Interpreting and Leveraging Semantic Information in Diffusion Models. In *Proceedings of the IEEE/CVF International Conference on Computer Vision*, pages 4659–4669, 2025. 1

[29] Zhifeng Kong, Wei Ping, Jiaji Huang, Kexin Zhao, and Bryan Catanzaro. DiffWave: A Versatile Diffusion Model for Audio Synthesis. *arXiv preprint arXiv:2009.09761*, 2020. 1

[30] Kaisa Kraft, Otso Velhonoja, Tuomas Eerola, Sanna Suikkanen, Timo Tamminen, Lumi Haraguchi, Pasi Ylöstalo, Sami Kielosto, Milla Johansson, Lasse Lensu, et al. Towards Operational Phytoplankton Recognition with Automated High-throughput Imaging, Near-Real-time Data Processing, and Convolutional Neural Networks. *Frontiers in Marine Science*, 9:867695, 2022. 5, 6, 12, 14

[31] Harold W Kuhn. The Hungarian Method for the Assignment Problem. *Naval Research Logistics Quarterly*, 2(1-2):83–97, 1955. 8

[32] Yan Li, Jiahong Guo, Xiaomin Guo, Zhiqiang Hu, and Yu Tian. Plankton Detection with Adversarial Learning and a Densely Connected Deep Learning Model for Class Imbalanced Distribution. *Journal of Marine Science and Engineering*, 9(6):636, 2021. 2

[33] Tsung-Yu Lin, Aruni RoyChowdhury, and Subhransu Maji. Bilinear CNN Models for Fine-grained Visual Recognition. In *Proceedings of the IEEE International Conference on Computer Vision*, pages 1449–1457, 2015. 2

[34] Jing Liu, Angang Du, Chao Wang, Haiyong Zheng, Nan Wang, and Bing Zheng. Teaching Squeeze-and-Excitation PyramidNet for Imbalanced Image Classification with GAN-based Curriculum Learning. In *2018 24th International Conference on Pattern Recognition (ICPR)*, pages 2444–2449. IEEE, 2018. 2

[35] G Lowe. SIFT (Scale-Invariant Feature Transform). *Int. j.*, 2 (91-110):2, 2004. 6

[36] Grace Luo, Lisa Dunlap, Dong Huk Park, Aleksander Holynski, and Trevor Darrell. Diffusion Hyperfeatures: Searching Through Time and Space for Semantic Correspondence. *Advances in Neural Information Processing Systems*, 36: 47500–47510, 2023. 1

[37] Gautam Mittal, Jesse Engel, Curtis Hawthorne, and Ian Simon. Symbolic Music Generation with Diffusion Models. *arXiv preprint arXiv:2103.16091*, 2021. 1

[38] Soumik Mukhopadhyay, Matthew Gwilliam, Vatsal Agarwal, Namitha Padmanabhan, Archana Swaminathan, Srinidhi Hegde, Tianyi Zhou, and Abhinav Shrivastava. Diffusion Models Beat GANs on Image Classification. *arXiv preprint arXiv:2307.08702*, 2023. 2

[39] Soumik Mukhopadhyay, Matthew Gwilliam, Yosuke Yamaguchi, Vatsal Agarwal, Namitha Padmanabhan, Archana Swaminathan, Tianyi Zhou, Jun Ohya, and Abhinav Shrivastava. Do Text-free Diffusion Models Learn Discriminative Visual Representations? In *European Conference on Computer Vision*, pages 253–272. Springer, 2024. 2

[40] Koichi Namekata, Amirmojtaba Sabour, Sanja Fidler, and Seung Wook Kim. EmerDiff: Emerging Pixel-level Semantic Knowledge in Diffusion Models. *arXiv preprint arXiv:2401.11739*, 2024. 3

[41] Alexander Quinn Nichol and Prafulla Dhariwal. Improved Denoising Diffusion Probabilistic Models. In *International Conference on Machine Learning*, pages 8162–8171. PMLR, 2021. 3, 17

[42] Robert J Olson and Heidi M Sosik. A Submersible Imaging-in-flow Instrument to Analyze Nano-and Microplankton: Imaging FlowCytobot. *Limnology and Oceanography: Methods*, 5(6):195–203, 2007. 1

[43] Maxime Oquab, Timothée Darcet, Théo Moutakanni, Huy Vo, Marc Szafraniec, Vasil Khalidov, Pierre Fernandez,

Daniel Haziza, Francisco Massa, Alaaeldin El-Nouby, Mahmoud Assran, Nicolas Ballas, Wojciech Galuba, Russell Howes, Po-Yao Huang, Shang-Wen Li, Ishan Misra, Michael Rabbat, Vasu Sharma, Gabriel Synnaeve, Hu Xu, Hervé Jegou, Julien Mairal, Patrick Labatut, Armand Joulin, and Piotr Bojanowski. DINOv2: Learning Robust Visual Features without Supervision, 2024. 4

[44] Eric C Orenstein, Oscar Beijbom, Emily E Peacock, and Heidi M Sosik. WHOI-Plankton-a Large Scale Fine Grained Visual Recognition Benchmark Dataset for Plankton Classification. *arXiv preprint arXiv:1510.00745*, 2015. 1, 6, 14

[45] Alec Radford, Luke Metz, and Soumith Chintala. Unsupervised Representation Learning with Deep Convolutional Generative Adversarial Networks. *arXiv preprint arXiv:1511.06434*, 2015. 2

[46] Olaf Ronneberger, Philipp Fischer, and Thomas Brox. U-Net: Convolutional Networks for Biomedical Image Segmentation. In *International Conference on Medical Image Computing and Computer-Assisted Intervention*, pages 234–241. Springer, 2015. 4

[47] Oriane Siméoni, Huy V Vo, Maximilian Seitner, Federico Baldassarre, Maxime Oquab, Cijo Jose, Vasil Khalidov, Marc Szafraniec, Seungeun Yi, Michaël Ramamonjisoa, et al. DINOv3. *arXiv preprint arXiv:2508.10104*, 2025. 2, 6

[48] Jascha Sohl-Dickstein, Eric Weiss, Niru Maheswaranathan, and Surya Ganguli. Deep Unsupervised Learning using Nonequilibrium Thermodynamics. In *Proceedings of the 32nd International Conference on Machine Learning*, pages 2256–2265, Lille, France, 2015. PMLR. 1, 3

[49] Jiaming Song, Chenlin Meng, and Stefano Ermon. Denoising Diffusion Implicit Models. *arXiv preprint arXiv:2010.02502*, 2020. 17

[50] Yang Song, Jascha Sohl-Dickstein, Diederik P Kingma, Abhishek Kumar, Stefano Ermon, and Ben Poole. Score-Based Generative Modeling through Stochastic Differential Equations. *arXiv preprint arXiv:2011.13456*, 2021. 1, 2, 3

[51] Nick Stracke, Stefan Andreas Baumann, Kolja Bauer, Frank Fundel, and Björn Ommer. CleanDIFT: Diffusion Features without Noise, 2025. 3

[52] Mingxing Tan and Quoc Le. EfficientNet: Rethinking Model Scaling for Convolutional Neural Networks. In *International Conference on Machine Learning*, pages 6105–6114. PMLR, 2019. 2, 6

[53] Luming Tang, Menglin Jia, Qianqian Wang, Cheng Perng Phoo, and Bharath Hariharan. Emergent Correspondence from Image Diffusion. *Advances in Neural Information Processing Systems*, 36:1363–1389, 2023. 3

[54] Anders Torstensson, Ann-Turi Skjervik, Malin Mohlin, Maria Karlberg, and Bengt Karlsson. SMHI IFCB Plankton Image Reference Library, 2024. Dataset, version 4. 2, 5, 12

[55] Patrick von Platen, Suraj Patil, Anton Lozhkov, Pedro Cuenca, Nathan Lambert, Kashif Rasul, and et al. Diffusers: State-of-the-Art Diffusion Models. GitHub repository, 2022. <https://github.com/huggingface/diffusers>. 17

[56] Chao Wang, Zhibin Yu, Haiyong Zheng, Nan Wang, and Bing Zheng. CGAN-Plankton: Towards Large-Scale Imbalanced Class Generation and Fine-Grained Classification. In *2017 IEEE International Conference on Image Processing (ICIP)*, pages 855–859. IEEE, 2017. 2

[57] Sanghyun Woo, Jongchan Park, Joon-Young Lee, and In So Kweon. CBAM: Convolutional Block Attention Module. In *Proceedings of the European Conference on Computer Vision (ECCV)*, pages 3–19, 2018. 2

[58] WoRMS Editorial Board. World Register of Marine Species (WoRMS), 2025. 12

[59] Lemeng Wu, Chengyue Gong, Xingchao Liu, Mao Ye, and Qiang Liu. Diffusion-based Molecule Generation with Informative Prior Bridges. *Advances in Neural Information Processing Systems*, 35:36533–36545, 2022. 1

[60] Weilai Xiang, Hongyu Yang, Di Huang, and Yunhong Wang. Denoising Diffusion Autoencoders are Unified Self-supervised Learners. In *Proceedings of the IEEE/CVF International Conference on Computer Vision*, pages 15802–15812, 2023. 1, 2, 3

[61] Xingyi Yang and Xinchao Wang. Diffusion Model as Representation Learner. In *Proceedings of the IEEE/CVF International Conference on Computer Vision*, pages 18938–18949, 2023. 2

[62] Zhongqi Yue, Jiankun Wang, Qianru Sun, Lei Ji, Eric I Chang, Hanwang Zhang, et al. Exploring Diffusion Time-steps for Unsupervised Representation Learning. *arXiv preprint arXiv:2401.11430*, 2024. 1

[63] Junyi Zhang, Charles Herrmann, Junhwa Hur, Luisa Polanía Cabrera, Varun Jampani, Deqing Sun, and Ming-Hsuan Yang. A Tale of Two Features: Stable Diffusion Complements DINO for Zero-Shot Semantic Correspondence. *Advances in Neural Information Processing Systems*, 36: 45533–45547, 2023. 3

[64] Junyi Zhang, Charles Herrmann, Junhwa Hur, Eric Chen, Varun Jampani, Deqing Sun, and Ming-Hsuan Yang. Telling Left from Right: Identifying Geometry-Aware Semantic Correspondence. In *Proceedings of the IEEE/CVF Conference on Computer Vision and Pattern Recognition*, pages 3076–3085, 2024. 3

[65] Zhengbang Zhu, Hanye Zhao, Haoran He, Yichao Zhong, Shenyu Zhang, Haoquan Guo, Tingting Chen, and Weinan Zhang. Diffusion Models for Reinforcement Learning: A Survey. *arXiv preprint arXiv:2311.01223*, 2023. 1

A. Dataset Details

In this section, we describe how we construct the plankton datasets used in our experiments. We begin by integrating the raw, separately annotated datasets obtained from the **SYKE** [30] and **SMHI** [54] Baltic monitoring programs, which sample plankton communities along the **Swedish coast**, into a single label space spanning all taxa. From this common label space, we then define the in-distribution datasets used for training and evaluation, including both a balanced and an unbalanced variant, and we present the two out-of-distribution datasets used to assess model generalization. We first detail the curation and class-harmonization procedure, explaining how taxonomic labels from the two sources are merged into common categories and how these categories are used to construct the balanced and unbalanced datasets. We conclude by describing the preprocessing pipeline applied to all images. All taxonomic assignments follow the World Register of Marine Species (WoRMS) [58], which we adopt as a standardized reference for marine organism nomenclature.

A central characteristic of these datasets is the variability in taxonomic resolution. The included class labels span **multiple taxonomic ranks**, ranging from *species* to *genus* and even *order*. This variation stems from the differing levels of detail visible in plankton images: some organisms display clear morphological features that enable confident species-level identification, while others are ambiguous and can only be classified at broader levels. This is especially relevant when using automated imaging systems such as the Imaging FlowCytobot (IFCB) instruments used by SYKE and SMHI.

To accommodate this variability, the dataset includes both precise labels (e.g., defined species names) and generalized taxonomic categories using the standard “sp.” and “spp.” conventions. These indicate that the exact species is unknown: *Genus sp.* refers to a single, unidentified species within a genus, while *Genus spp.* refers to a group of species within the same genus. These broader categories ensure that valuable samples are not excluded due to taxonomic uncertainty.

A.1. Source Data and Taxonomic Harmonization

We construct our datasets from IFCB region-of-interest (ROI) image catalogs curated by the SMHI and SYKE Baltic monitoring programs. IFCB instruments acquire grayscale ROI images, i.e., cropped fields of view centered on individual particles (such as plankton cells, colonies, or detrital aggregates), along with expert-provided taxonomic labels maintained in each provider’s taxonomy.

To obtain consistent supervision across providers, we first harmonize the SMHI and SYKE taxonomies by collapsing synonymous labels and resolving provider-specific naming conventions. From the intersection of these harmonized taxonomies, we derive two datasets that share the same preprocessing pipeline but differ in class-frequency structure (balanced vs. naturally long-tailed).

The merged dataset was constructed by integrating four annotated image datasets: three provided by SMHI and one by SYKE.

- smhi_ifcb_baltic_annotated_images (1)
- smhi_ifcb_skagerrak_kattegat_annotated_images (2)
- smhi_ifcb_t_ngesund_annotated_images (3)
- phytoplankton_labeled_SYKE (4)

The three SMHI datasets (1-3) were first merged by aligning their folder structures and class names, which followed a consistent naming convention. After this unified SMHI dataset was created, the SYKE dataset (4) was merged in. While several class names matched exactly and were merged directly, others required taxonomic harmonization or renaming. The following decisions were taken during this process:

- *Gonyaulax_verior* (4) was merged with *Gonyaulax_spp* (2) under the name *Gonyaulax_verior*.
- *Licmophora_sp* (4) was merged with *Licmophora* (2) under *Licmophora_sp*.
- *Nodularia_spumigena* (4), which included both coiled and filamentous forms, was merged with *Nodularia_spumigena_coil* and *Nodularia_spumigena_filament* (1). The resulting class was named *Nodularia_spumigena_coil*.

- `centrales_sp` (4) was merged with `Centrales` (1,2). Notably, SYKE samples sometimes contained multiple planktonic elements, while SMHI samples generally showed single elements.
- `Oocystis_sp` (4) was merged with `Oocystis_spp` (1) under `Oocystis_sp`.
- `Monoraphidium_contortum` (4) was merged with `Monoraphidium_spp` (1) under `Monoraphidium_contortum`.
- `Pennales_sp_thick` (4) was merged into `Pennales`.
- `Peridiniella_catenata` (1) was merged with `Peridiniella_catenata_chain` and `Peridiniella_catenata_single` (4).
- `Eutreptiella_sp` (4) was merged with `Eutreptiella_spp` (1,2,3) under `Eutreptiella_spp`.
- `Cyclotella_chocatawhatcheeana` (4) was merged into `Cyclotella_spp` (1) under `Cyclotella_chocatawhatcheeana`.
- `Chaetoceros_sp` (4) was merged with `Chaetoceros_spp` (3).
- `Chaetoceros_sp_single` (4) was merged with `Chaetoceros_single_cell` (1).
- `ciliata` (4) was merged with `ciliates` (2), adopting the taxonomically correct label `Ciliata` according to WoRMS.

A.2. Balanced and Unbalanced Datasets

From the curated dataset obtained in Section A.1, we derive two datasets that we use to train our diffusion models.

Balanced dataset. To obtain a controlled benchmark focused on representation quality, we first select all classes that have at least 100 labeled images in the curated dataset, which leaves us with $k = 70$ classes. For each of these k classes, we then construct a dataset by randomly sampling up to 500 single-channel grayscale images per class. We first perform a class-stratified split into training, validation, and test sets with an 80/10/10 ratio, yielding up to 400, 50, and 50 images per class, respectively. We then enforce class balance in the training split by ensuring that each class contributes exactly 400 samples. For classes that had fewer than 500 samples in the original curated dataset, we obtain the missing training samples by augmenting only the training split, leaving the validation and test sets unaugmented. Each augmented training image is generated by applying a single geometric transformation at a time to a real training image: horizontal flip, vertical flip, 180° rotation, or uniform color intensity scaling by -10% , -5% , $+5\%$, or $+10\%$.

Unbalanced (long-tailed) dataset. To mirror realistic monitoring conditions, we construct an unbalanced dataset starting from the curated dataset. We first remove classes with fewer than 5 labeled images, as such classes are too small to be informative for training or evaluation. After this filtering step, we are left with 120 classes. For each of these classes, we then include all available images that pass the preprocessing and quality-control steps described in Section A.4, without imposing any further per-class subsampling. As in the balanced setting, we perform a class-stratified split into training, validation, and test sets using an 80/10/10 ratio. However, unlike in the balanced case where we explicitly enforce 400 training samples per class, here rare classes may contribute only a handful of training images, and even when we apply the same set of simple geometric augmentations used in the balanced case (horizontal flip, vertical flip, 180° rotation, and uniform color intensity scaling by -10% , -5% , $+5\%$, or $+10\%$) only to the training split, their effective training size remains far below 400 samples. As a result, the training set is heavily long-tailed, with a few abundant classes and many rare species, closely matching the operational scenario in automated plankton monitoring.

Splits usage. The diffusion model is trained *only* on the training split, without labels. The validation split is non-augmented and used to track diffusion loss, monitor generative quality via FID, and select the layer-timestep pair for the linear probe. The held-out test split is a fixed, non-augmented subset used exclusively for downstream evaluation, where we report test accuracy and Macro F1 for the linear classifier trained on frozen diffusion features.

A.3. Out-of-Distribution Test Sets

We assess distribution robustness on two unseen IFCB datasets by freezing the diffusion backbone and training a linear probe on an 80/20 target train/test split, then reporting Accuracy and Macro F1 on the target test set.

Baltic (OOD). The first out-of-distribution (OOD) dataset is a year-long Baltic Sea collection from 2021 [30], acquired over a 12-month period that is disjoint from the years used for the SMHI and SYKE data employed to construct our balanced and unbalanced source datasets. It reflects the realistic distribution of Baltic plankton across the full annual cycle, from ice-affected winter conditions to spring and summer blooms, and thus provides a natural, unsorted, and robust testbed for validating our models under temporal and environmental shifts. For this dataset, we freeze the diffusion backbone trained on either the 70-class balanced or the 120-class unbalanced source regime, extract features, and train only a linear classifier on Baltic labels. The diffusion model is never exposed to this Baltic collection during training, so it is used purely as an out-of-distribution test set. When mapping Baltic labels to the source taxonomies, all Baltic classes are covered by the 120-class unbalanced source dataset, whereas the 70-class balanced source dataset lacks three Baltic taxa: *Aphanothecae_paralleliformis*, *Licmophora_sp*, and *Melosira_arctica*.

WHOI-22. The second OOD dataset, WHOI-22 [44], is a curated subset of the WHOI-Plankton benchmark acquired on the U.S. Atlantic coast using IFCB instrumentation. It differs from the Baltic data in geography, community composition, and acquisition conditions, and includes taxa not present in our Baltic source datasets. As with the Baltic (OOD) set, we evaluate by freezing the diffusion backbone trained on the Baltic balanced or unbalanced regime and fitting a linear classifier on top of the extracted features. As in the Baltic OOD dataset, the diffusion backbone is never exposed to target-domain images. When mapping WHOI-22 labels to the Baltic source taxonomies, several WHOI-22 taxa are not covered by one or both source regimes: the 120-class unbalanced dataset lacks *DactFragCeratul*, *Euglena*, *Phaeocystis*, *Pleurosigma*, *detritus*, *nanoflagellate*, *other_lt20*, and *pennate*, and the 70-class balanced dataset additionally lacks *Asterionellopsis*, *Cylindrotheca*, *Dinobryon*, *Ditylum*, and *Licmophora_sp*. The full overlap pattern is summarized in Table 3.

Table 3. Taxa in WHOI-22 that are *not covered* by at least one of the two Baltic source taxonomies (120-class unbalanced and 70-class balanced). “Yes” indicates that the taxon is present in the corresponding source dataset; “No” indicates it is absent.

WHOI-22 taxon	120-class unbalanced	70-class balanced
<i>Asterionellopsis</i>	Yes	No
<i>Cylindrotheca</i>	Yes	No
<i>DactFragCeratul</i>	No	No
<i>Dinobryon</i>	Yes	No
<i>Ditylum</i>	Yes	No
<i>Euglena</i>	No	No
<i>Licmophora_sp</i>	Yes	No
<i>Phaeocystis</i>	No	No
<i>Pleurosigma</i>	No	No
<i>detritus</i>	No	No
<i>nanoflagellate</i>	No	No
<i>other_lt20</i>	No	No
<i>pennate</i>	No	No

A.4. Preprocessing Pipeline

All curation and preprocessing precede any model training and are applied identically to the training, validation, test, and OOD partitions. The pipeline mapping raw IFCB ROIs to standardized recognition images is fully deterministic.

- File integrity and metadata checks.** We discard corrupt images and zero-sized files. Each class name is assigned to a unique integer class identifier to ensure one-to-one label indices across SMHI and SYKE.
- Grayscale standardization.** IFCB images are inherently single-channel. Any multi-channel encodings are converted to a single channel via luminance, and intensities are linearly rescaled to $[0, 1]$.
- Resizing.** Each ROI is resized to a 128×128 square without padding. In preliminary experiments, we evaluated several padding strategies, but pure resizing yielded the most reliable downstream performance for our U-Net-based diffusion model, so we adopt it throughout. However, a systematic study of padding and resizing schemes for plankton data remains an open challenge.

A.5. Augmentations

Across both the balanced and unbalanced source regimes, we adopt a deliberately conservative augmentation strategy that is applied *only* to the training split. In both cases, augmented samples are generated from real ROIs using the same small set of label-preserving geometric transformations: horizontal flip, vertical flip, 180° rotation, and uniform color intensity scaling by -10% , -5% , $+5\%$, or $+10\%$, with a single transformation applied per original image. In the balanced regime, this allows us to synthetically increase underrepresented classes so that each class contributes exactly 400 training examples, while leaving the validation and test splits unchanged. In the unbalanced, long-tailed regime, the same augmentations modestly strengthen supervision for rare taxa without coming close to equalizing class frequencies, so the training distribution remains heavily long-tailed.

We restrict ourselves to these simple geometric operations because they encode natural invariances of IFCB imagery: the orientation of the organism in the flow cell is arbitrary, and slight changes in apparent size are common due to focus and segmentation variability, whereas more aggressive manipulations (such as strong cropping or elastic deformations) could distort morphological cues that are important for taxonomic identity. Applying augmentations exclusively to the training split ensures that the validation, test, and OOD datasets consist solely of real, preprocessed ROIs, so that all reported performance reflects behavior on realistic acquisition conditions while still benefiting from an increased effective sample size during model training.

Table 4. List of the plankton species in our balanced dataset.

Alexandrium_pseudogonyaulax	Gymnodinium_like
Aphanizomenon_flosaqueae	Heterocapsa_rotundata
Aphanizomenon_spp_bundle	Heterocapsa_triquetra
Aphanizomenon_spp_filament	Heterocyte
Asterionellopsis_glacialis	Leptocylindrus_danicus
Beads	Leptocylindrus_danicus_minimus
Centrales	Lingulodinium_polyedrum
Cerataulina_pelagica	Mesodinium_rubrum
Chaetoceros_chain	Monoraphidium_contortum
Chaetoceros_single_cell	Nodularia_spumigena
Chaetoceros_spp	Octactis_speculum
Chroococcales	Oocystis_sp
Chroococcus_small	Oscillatoriaceae
Ciliata	Pauliella_taeniata
Cryptomonadales	Pennales_sp_thick
Cryptophyceae_Teleaulax	Pennales_sp_thin
Cyclotella_chocawhatcheeana	Peridiniella_catenata_chain
Cylindrotheca_Nitzschia_longissima	Peridiniella_catenata_single
Cymbomonas_tetramitiformis	Prorocentrum_cordatum
Dactyliosolen_fragilissimus	Prorocentrum_micans
Diatoma_tenuis-like_chain	Prorocentrum_triestinum
Diatoma_tenuis-like_single_cell	Pseudo_nitzschia_spp
Dictyocha_naked	Pseudopedinella_sp
Dino_smaller_than_30unidentified	Pseudosolenia_calcar_avis
Dinophyceae	Pyramimonas_sp
Dinophysis_acuminata	Rhizosolenia_Pseudosolenia
Dolichospermum_Anabaenopsis	Scrippsiella_CPX
Dolichospermum_Anabaenopsis_coiled	Scrippsiella_group
Dolichospermum_spp_coil	Skeletonema_marinoi
Dolichospermum_spp_filament	Snowella_Woronichinia
Euglenophyceae	Strombidium_like
Eutreptiella_spp	Thalassiosira_gravida
Guinardia_delicatula	Thalassiosira_levanderi
Gymnodiniales	Tripos_lineatus
Gymnodiniales_smaller_than_30	Uroglenopsis_sp

Table 5. List of the plankton species in our unbalanced dataset, including the number of samples per class.

Alexandrium_pseudogonyaulax	387	Gyrodinium_spirale	65
Amphidinium_like	40	Gyrosigma_Pleurosigma	40
Amylax_triacantha	146	Heterocapsa_rotundata	550
Apedinella_radians	307	Heterocapsa_triquetra	550
Aphanizomenon_flosaqueae	550	Heterocyte	513
Aphanizomenon_spp_bundle	407	Karenia_mikimotoi	315
Aphanizomenon_spp_filament	550	Katablepharis_remigera	304
Aphanothecae_paralleliformis	211	Katodinium_like	268
Asterionellopsis_glacialis	550	Leptocylindrus_danicus	380
Beads	375	Leptocylindrus_danicus_minimus	396
Binuclearia_lauterbornii	297	Licmophora_sp	325
Centrales	550	Lingulodinium_polyedrum	550
Cerataulina_pelagica	351	Melosira_arctica	293
Ceratoneis_closterium	295	Merismopedia_sp	348
Chaetoceros_cf_convolutus	344	Mesodinium_major	319
Chaetoceros_chain	360	Mesodinium_rubrum	550
Chaetoceros_danicus	302	Monoraphidium_contortum	535
Chaetoceros_single_cell	522	Nitzschia_paleacea	315
Chaetoceros_spp	550	Nodularia_spumigena	537
Chaetoceros_wighamii	195	Octactis_speculum	363
Chlorococcales	345	Oocystis_sp	550
Chroococcales	392	Oscillatoriales	550
Chroococcus_small	550	Pauliella_taeniata	369
Ciliata	534	Pennales_sp_thick	494
Ciliophora	315	Pennales_sp_thin	550
Cryptomonadales	550	Peridiniales_smaller_than_30	89
Cryptophyceae_Teleaulax	550	Peridiniella_catenata_chain	478
Cyclotella_chocatawhatcheeana	462	Peridiniella_catenata_single	550
Cylindrotheca_Nitzschia_longissima	453	Proboscia_alata	41
Cymbomonas_tetramitiformis	449	Prorocentrum_cordatum	532
Dactyliosolen_fragilissimus	533	Prorocentrum_micans	550
Diatoma_tenuis-like_chain	550	Prorocentrum_triestinum	550
Diatoma_tenuis-like_single_cell	545	Pseudo_nitzschia_spp	550
Dictyocha_fibula	81	Pseudopedinella_sp	538
Dictyocha_naked	550	Pseudosolenia_calcar_avis	403
Dino_larger_than_30unidentified	327	Pyramimonas_sp	550
Dino_smaller_than_30unidentified	544	Rhizosolenia_Pseudosolenia	387
Dinobryon_spp	332	Rhizosolenia_hebetata_f_semispina	40
Dinoflagellate_smaller_than_30	146	Rhizosolenia_setigera	298
Dinophyceae	550	Scenedesmus_spp	162
Dinophysis_acuminata	538	Scrippsiella_CPX	550
Dinophysis_norvegica	260	Scrippsiella_group	517
Ditylum_brightwellii	327	Skeletonema_marinoi	550
Dolichospermum_Anabaenopsis	550	Snowella_Woronichinia	550
Dolichospermum_Anabaenopsis_coiled	550	Strombidium_like	550
Dolichospermum_spp_coil	550	Thalassionema_nitzschiooides	203
Dolichospermum_spp_filament	550	Thalassiosira_anguste-lineata	41
Double_cells	307	Thalassiosira_gravida	363
Ebria_tripartita	41	Thalassiosira_levanderi	550
Ensiculifera_carinata	97	Thalassiosira_nordenskioeldii	334
Euglenophyceae	352	Thalassiosira_punctigera	73
Eutreptiella_spp	550	Thalassiosira_spp	308
Gonyaulax_spinifera	81	Torodinium_robustum	347
Gonyaulax_verior	170	Tripos_furca	146
Guinardia_delicatula	550	Tripos_fusus	57
Guinardia_flaccida	57	Tripos_lineatus	429
Gymnodiniales	532	Tripos_muelleri	122
Gymnodiniales_smaller_than_30	474	Uroglenopsis_sp	550
Gymnodinium_like	408	Warnowia_like	113

B. Implementation and Reproducibility

To enable faithful replication and extension of our results, this section specifies the exact model components and training/evaluation settings we use. We describe implementation choices at the level needed to re-run experiments end-to-end, including architectural details and hyperparameters.

B.1. Full U-Net Architecture

We use a DDPM-style U-Net denoiser E_θ implemented in `diffusers` (`UNet2DModel`) operating on single-channel 128×128 inputs. The U-Net encoder channel pattern is [64, 128, 256, 512]; the decoder mirrors these widths with skip connections. Residual blocks are pre-activation with `GroupNorm(16)` and `SiLU`, and no cross-attention is used. We use *self-attention* only at the 16×16 stage (after the last residual block in both encoder and decoder), as this mid-resolution offers a good trade-off between receptive field, spatial detail, and downstream feature quality, in line with prior analyses of diffusion backbones and intermediate noise scales [9, 15].

Table 6. U-Net configuration (Diffusers).

Configuration	Value
Architecture	DDPM-style U-Net denoiser (<code>UNet2DModel</code>) [55].
Channel multipliers	$1-2-4-8$ (stages at $128^2, 64^2, 32^2, 16^2$).
Attention resolutions	$\{16\}$ (self-attention only at 16×16 —both encoder and decoder).
Blocks per resolution	encoder = 2, bottleneck = 2, decoder = 3.
Normalization	<code>GroupNorm(16)</code> .
Activation	<code>SiLU</code> .
Params	$\sim 57M$.

B.2. Training Details and Compute

We optimize the ϵ -prediction objective presented in the main article with `MinSNR- γ` weighting:

$$w(t) = \frac{\min(\text{SNR}(t), \gamma)}{\text{SNR}(t)}, \quad \gamma = 5, \quad (18)$$

which rebalances over/under-weighted timesteps and improves sample efficiency [18]. We use the cosine $\bar{\alpha}_t$ noise schedule with offset $s = 0.008$ [41], and we draw timesteps from a *squared-cosine* importance distribution aligned with this schedule. For qualitative sampling and evaluation, we use DDIM with 100 steps, $\eta = 0$ (deterministic) [49]. Mixed precision training runs on a single node with $4 \times$ A100-40GB using `accelerate` and `DDP` [55].

Table 7. Training setup (Diffusers).

Config	Value
Optimizer	<code>AdamW</code> ; $\beta_1 = 0.9, \beta_2 = 0.999$, decay $1e-4$; grad. clip = 1.0.
Base learning rate	$5e-4$; cosine decay with 5% warmup.
Batch size per GPU	64 (global 256 over 4 GPUs).
Noise schedule	cosine $\bar{\alpha}_t$ with offset $s = 0.008$ [41].
t -sampling distribution	squared-cosine importance over timesteps (in line with the schedule).
Loss weighting	<code>MinSNR-γ</code> with $\gamma = 5$ [18].
Sampler (eval)	DDIM, 100 steps, $\eta = 0$ [49].
Epochs	250.

Compute and Runtime. Training uses $4 \times$ A100-40GB on a single node with `fp16`; peak memory per process is ~ 38 GB and the 250-epoch run took 15 hours in total.

B.3. Hyperparameters for Probes and Clustering

We list the exact configurations used for linear probing and k -means clustering; all hyperparameters and implementation details for linear probe are given in Table 8.

Table 8. Linear probe hyperparameters.

Config	Value
Classifier	Linear softmax classifier, PyTorch.
Features	GAP-pooled decoder activations at (t, ℓ) ; ℓ_2 -normalized.
Loss	Cross-entropy, label smoothing = 0.0.
Optimizer	Adam; lr = 1e-3; betas = (0.9, 0.999); weight decay = 5e-4.
Epochs	10.
Batch size	512.
Regularization	None.

For k -means clustering and retrieval (using features at (t^*, ℓ^*) on the test split), we set $k = 70$. The algorithm uses `n_init` = 5 restarts and a maximum of 300 iterations per run, with a convergence tolerance of 1×10^{-4} . When class labels are required, clusters are mapped to classes by majority vote.

C. Extended Results

This section provides additional experimental results that complement those presented in the main paper. The goal is completeness and clarity, without revisiting interpretations already covered in the main text.

C.1. Linear Probe

The linear-probe results across all decoder readout locations and timesteps are reported in Tables 9 and 10, respectively. We report timesteps up to $t = 100$ since our sweep indicates that performance peaks at low noise (e.g., $t^* = 25$) and drops sharply at higher noise levels; including larger t values provides little additional insight while increasing feature-extraction cost.

Table 9. Linear probe test results across decoder stages and denoising timesteps t . Each cell reports *Accuracy / Macro F1*. Rows list the three *residual blocks* (RB1 to RB3) at each resolution; attention is used at 16^2 . For each timestep t , the best entry appears in **black**. The selected operating point (t^*, ℓ^*) , where ℓ denotes the readout location (resolution \times residual block), is highlighted in **red**. *Balanced dataset*.

Resolution	Residual Block	Denoising timestep t (Accuracy \uparrow / Macro F1 \uparrow)					
		1	10	25	50	75	100
16^2 (attn)	RB1	0.8955 / 0.8822	0.8925 / 0.8793	0.8890 / 0.8780	0.8829 / 0.8668	0.8945 / 0.8821	0.8910 / 0.8780
	RB2	0.9133 / 0.9062	0.9058 / 0.9021	0.9071 / 0.9022	0.9090 / 0.9001	0.9086 / 0.8974	0.9089 / 0.9004
	RB3	0.9213 / 0.9101	0.9191 / 0.9137	0.9240 / 0.9114	0.9163 / 0.9112	0.9159 / 0.9086	0.9169 / 0.9098
32^2	RB1	0.9105 / 0.9044	0.9082 / 0.8942	0.9076 / 0.8993	0.9181 / 0.9087	0.9079 / 0.9030	0.9057 / 0.9003
	RB2	0.9019 / 0.8915	0.8991 / 0.8900	0.9138 / 0.8881	0.9157 / 0.9079	0.9132 / 0.9011	0.8987 / 0.8946
	RB3	0.9017 / 0.8925	0.8971 / 0.8801	0.9114 / 0.9050	0.9098 / 0.8964	0.9146 / 0.9067	0.9099 / 0.9033
64^2	RB1	0.8607 / 0.8464	0.8599 / 0.8612	0.8574 / 0.8670	0.8703 / 0.8629	0.8780 / 0.8691	0.8763 / 0.8655
	RB2	0.8079 / 0.7908	0.8090 / 0.7880	0.8169 / 0.7893	0.8307 / 0.8081	0.8314 / 0.8112	0.8268 / 0.8092
	RB3	0.7495 / 0.7189	0.7512 / 0.7321	0.7212 / 0.7478	0.7806 / 0.7600	0.7895 / 0.7641	0.7898 / 0.7659
128^2	RB1	0.5924 / 0.5428	0.5919 / 0.5492	0.5937 / 0.5432	0.6115 / 0.5725	0.6014 / 0.5462	0.5774 / 0.5241
	RB2	0.5513 / 0.4887	0.5243 / 0.4570	0.5095 / 0.4442	0.4807 / 0.3952	0.4522 / 0.3802	0.4464 / 0.3831
	RB3	0.4978 / 0.4162	0.4380 / 0.3790	0.4144 / 0.3342	0.3412 / 0.2752	0.3228 / 0.2542	0.3013 / 0.2350

Table 10. Linear probe test results across decoder stages and denoising timesteps t . Each cell reports *Accuracy / Macro F1*. Rows list the three *residual blocks* ($RB1$ to $RB3$) at each resolution; attention is used at 16^2 . For each timestep t , the best entry appears in **black**. The selected operating point (t^*, ℓ^*) , where ℓ denotes the readout location (resolution \times residual block), is highlighted in **red**. *Unbalanced dataset*.

Resolution	Residual Block	Denoising timestep t (Accuracy \uparrow / Macro F1 \uparrow)					
		1	10	25	50	75	100
16^2 (attn)	$RB1$	0.8535 / 0.8453	0.8512 / 0.8474	0.8582 / 0.8488	0.8508 / 0.8434	0.8582 / 0.8499	0.8526 / 0.8426
	$RB2$	0.8873 / 0.8798	0.8877 / 0.8802	0.8886 / 0.8813	0.8833 / 0.8785	0.8797 / 0.8723	0.8778 / 0.8702
	$RB3$	0.9052 / 0.8974	0.9034 / 0.8992	0.9145 / 0.9064	0.8998 / 0.8931	0.8938 / 0.8873	0.8899 / 0.8822
32^2	$RB1$	0.8965 / 0.8903	0.8961 / 0.8892	0.8957 / 0.8887	0.8975 / 0.8913	0.8958 / 0.8898	0.8930 / 0.8875
	$RB2$	0.8737 / 0.8641	0.8739 / 0.8942	0.8819 / 0.8728	0.8871 / 0.8777	0.8900 / 0.8795	0.8821 / 0.8728
	$RB3$	0.8687 / 0.8597	0.8710 / 0.8629	0.8777 / 0.8697	0.8819 / 0.8751	0.8864 / 0.8788	0.8803 / 0.8730
64^2	$RB1$	0.8276 / 0.8156	0.8312 / 0.8291	0.8477 / 0.8378	0.8400 / 0.8307	0.8477 / 0.8396	0.8543 / 0.8446
	$RB2$	0.7633 / 0.7512	0.7713 / 0.7560	0.7775 / 0.7594	0.7812 / 0.7629	0.7773 / 0.7603	0.7861 / 0.7733
	$RB3$	0.7219 / 0.7043	0.7389 / 0.7230	0.7525 / 0.7332	0.7483 / 0.7286	0.7532 / 0.7329	0.7615 / 0.7454
128^2	$RB1$	0.5601 / 0.5166	0.5518 / 0.5102	0.5499 / 0.5052	0.5613 / 0.5191	0.5564 / 0.5103	0.5586 / 0.5138
	$RB2$	0.4760 / 0.4235	0.4732 / 0.4199	0.4715 / 0.4192	0.4533 / 0.3994	0.4568 / 0.4016	0.4537 / 0.3997
	$RB3$	0.3603 / 0.2923	0.3333 / 0.2701	0.2924 / 0.2219	0.2449 / 0.1834	0.2159 / 0.1589	0.2152 / 0.1523

C.2. Clustering

Table 11 reports clustering performance for the U-Net and CNN runs. These metrics are not the result of hyperparameter tuning; rather, they provide a preliminary assessment of representation quality, indicating whether unsupervised clustering is likely to succeed and whether the embedding geometry exhibits class-consistent cohesion and separation. *As the CNN runs are trained with labeled data, stratified by the true plankton classes, they obtain stronger clustering metrics.* By contrast, the U-Net results demonstrate the promising direction of diffusion models for fine-grained representation learning, consistent with the patterns observed in the clustering figure presented in the main article.

Table 11. Clustering quality at the selected (t^*, ℓ^*) with $k = 70$ clusters. Arrows indicate higher is better. *NMI* is mutual information normalized to $[0, 1]$; *ARI* is agreement corrected for chance; *Purity* is the fraction assigned to the majority true class within each cluster; *V-measure* is the harmonic mean of homogeneity and completeness; *Silhouette* is the mean coefficient in $[-1, 1]$ measuring cohesion vs. separation. Results averaged over 5 k -means runs.

Regime	Run	NMI \uparrow	ARI \uparrow	Purity \uparrow	V-measure \uparrow	Silhouette \uparrow
Balanced	U-Net	0.8688	0.7354	0.8401	0.8642	0.2766
	ResNet 50 (CNN)	0.8802	0.7918	0.8852	0.8801	0.3067
	EfficientNet B0 (CNN)	0.9288	0.9005	0.9219	0.9188	0.4334
Unbalanced	U-Net	0.8450	0.7120	0.7950	0.8500	0.2750
	ResNet 50 (CNN)	0.8675	0.7629	0.8721	0.8671	0.2932
	EfficientNet B0 (CNN)	0.9100	0.8950	0.9180	0.9080	0.4150

C.3. Generation Quality and Overfitting

Figure 5 illustrates how the diffusion model starts to overfit as training progresses. While the training loss (red) continues to decrease monotonically, the validation loss (blue) reaches a minimum and then slowly increases, indicating a loss of generalization. In contrast, the FID score (black, right axis) keeps improving throughout training, meaning that the visual quality of generated samples becomes better even as the model begins to overfit the training distribution, since train and validation distributions differ only mildly due to low intra-class variability. The boxed region around epoch 100 marks the regime where this discrepancy is most evident: the FID is already substantially improved compared to early epochs, but the validation loss has stopped decreasing and begins to drift upward, and further training no longer translates into better performance of the linear probe on downstream classification. For this reason, we selected an early-stopping point at 100 epochs, which balances generation quality and representation quality rather than optimizing FID alone.

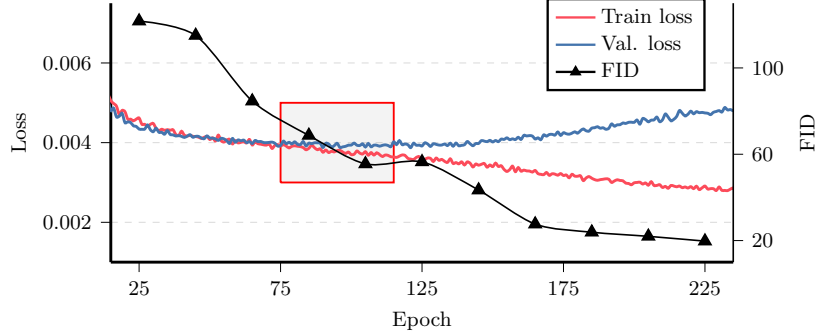


Figure 5. Training and validation loss (left axis) and Fréchet Inception Distance (FID, right axis) on the validation set as a function of epoch for the diffusion model. FID is computed from 10k generated samples compared to the validation set, with grayscale ROIs replicated to three channels for Inception-V3.

C.4. Motivation Behind MinSNR- γ Loss Function

Training diffusion models with the standard MSE loss induces a strong bias toward low-noise timesteps, where the model is almost reconstructing clean images. This effect originates from the interaction between the noise schedule and the objective: timesteps with a high signal-to-noise ratio automatically receive larger effective weights in the loss, and the corresponding gradients are larger whenever the model makes an error on nearly clean inputs. As a result, these timesteps dominate the optimization, and the network is primarily driven to refine tiny pixel-level corrections around already clean images.

This optimization bias has important consequences for representation learning. When supervision is concentrated on almost clean inputs, the model can rely on very fine, instance-specific details: background texture, small sensor artifacts, or subtle color variations that happen to correlate with the label in the training set. Such cues are easy to exploit at low noise, but they are not stable under moderate corruption or distribution shift. The learned embeddings, therefore, tend to encode brittle, image-specific information rather than robust, class-level structure, which limits generalization in fine-grained classification, especially when images are perturbed.

In contrast, the proposed MinSNR- γ loss with $\gamma = 5$ explicitly counteracts this bias by reshaping the learning signal across timesteps. Instead of allowing high-SNR (low-noise) inputs to dominate the gradients, it down-weights very clean timesteps and amplifies the contribution of a band of mid-noise timesteps, where the input is still semantically recognizable but low-level pixel cues have largely been suppressed. To perform well in this regime, the model must rely on features that summarize stable, class-relevant structure (e.g., the shape and configuration of object parts) rather than idiosyncratic texture or background artifacts. Empirically, this reweighting leads to more robust representations: in our experiments, MinSNR- γ preserves downstream classification performance under moderate corruption, whereas models trained with the standard MSE objective exhibit a marked degradation in that regime.

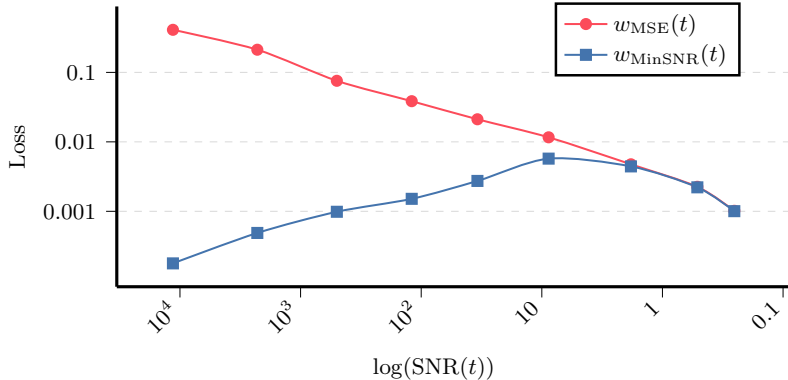


Figure 6. Mean-squared denoising loss of the U-Net as a function of the signal-to-noise ratio (SNR). The loss remains low at high SNR and increases sharply as γ decreases, indicating that the model struggles to reconstruct highly noisy inputs.

Figure 6 illustrates how this mechanism manifests in practice by plotting the per-timestep denoising loss of a U-Net as a function of the signal-to-noise ratio. Under the standard MSE objective (blue curve), the loss is largest for very high SNR values, confirming that optimization is dominated by nearly clean inputs. In contrast, the $\text{MinSNR-}\gamma$ objective (red curve) strongly suppresses the loss in this high-SNR regime and instead concentrates the effective training signal in an intermediate band of SNR values, where the inputs are noisy yet still semantically informative. Even if the normalized per-timestep loss curves appear superficially similar, the aggregate objective integrates them with different timestep-dependent weights, so that $\text{MinSNR-}\gamma$ yields a more balanced training signal whose gradients are better aligned with the requirements of downstream classification across a range of noise levels.